

## LA-UR-19-29326

Approved for public release; distribution is unlimited.

Title: Comparison of mechanical testing across micro- and meso- length scales

Author(s): Gigax, Jonathan Gregory  
Torrez, Avery Jude  
Mcculloch, Quinn  
Li, Nan

Intended for: Report

Issued: 2019-09-17

---

**Disclaimer:**

Los Alamos National Laboratory, an affirmative action/equal opportunity employer, is operated by Triad National Security, LLC for the National Nuclear Security Administration of U.S. Department of Energy under contract 89233218CNA000001. By approving this article, the publisher recognizes that the U.S. Government retains nonexclusive, royalty-free license to publish or reproduce the published form of this contribution, or to allow others to do so, for U.S. Government purposes. Los Alamos National Laboratory requests that the publisher identify this article as work performed under the auspices of the U.S. Department of Energy. Los Alamos National Laboratory strongly supports academic freedom and a researcher's right to publish; as an institution, however, the Laboratory does not endorse the viewpoint of a publication or guarantee its technical correctness.

# ***Comparison of mechanical testing across micro- and meso- length scales***

**Fuel Cycle Research & Development**

***Prepared for  
U.S. Department of Energy  
Advanced Fuels Campaign***

***Jonathan G. Gigax  
Avery J. Torrez  
Quinn McCulloch  
Nan Li***



**09/12/19**

#### **DISCLAIMER**

Los Alamos National Laboratory, an affirmative action/equal opportunity employer, is operated by Triad National Security, LLC, for the National Nuclear Security Administration of the U.S. DOE under contract 89233218CNA000001. By approving this article, the publisher recognizes that the U.S. Government retains nonexclusive, royalty-free license to publish or reproduce the published form of this contribution, or to allow others to do so, for U.S. Government purposes. Los Alamos National Laboratory requests that the publisher identify this article as work performed under the auspices of the U.S. Department of Energy. Los Alamos National Laboratory strongly supports academic freedom and a researcher's right to publish; as an institution, however, the Laboratory does not endorse the viewpoint of a publication or guarantee its technical correctness.

## SUMMARY

The present report summarizes the results from a variety of tests performed across different lengths scales used to evaluate the mechanical properties of a FeCrAl C26M weld. A variety of microscale and mesoscale mechanical tests were performed to evaluate a range of properties including nanoindentation hardness, compression and shear yield strengths, tensile strengths, and elongation. Using the mesoscale tensile testing as a baseline for comparison, micropillar compression was found to be the most sensitive to microstructural changes in the weld. Nanoindentation hardness testing, being high throughput, is recommended as a first step to identify major changes in the system and if residual stress is present.

## TABLE OF CONTENTS

SUMMARY .....	iv
1. Introduction .....	1
2. Materials and Methods .....	2
3. Results and Discussion .....	3
3.1 Microstructure of the FeCrAl weld .....	3
3.2 Nanoindentation hardness and modulus profiling.....	4
3.3 Spherical Nanoindentation .....	5
3.4 Micropillar Compression .....	7
3.5 Microshear Compression .....	8
3.6 Microshear Compression .....	10
3.7 Microshear Compression .....	12
4. Conclusions and Future Work .....	15
5. References .....	16

## FIGURES

Figure 1 - EBSD pole figure map of the C26M weld .....	3
Figure 2 - (a) Hardness and (b) Modulus depth profiles obtained from Berkovich nanoindentation in the fusion zone, tube heat-affect zone, and tube base material. (c) Hardness and (d) Modulus profiles across the C26M weld averaged between a depth of 400 nm to 500 nm. ....	5
Figure 3 - Spherical Nanoindentation stress-strain curves for the (a) tube and (b) plug side of the weld. ....	6
Figure 4 - Micropillar in the fusion zone (a) before and (b) after compression. Micropillar stress-strain curves for the (a) tube and (b) plug side. ....	8
Figure 5 - Single shear (a) before and (b) after compression, and (c) representative shear stress-strain curves for each region. Double shear (d) before and (e) after compression, and (f) representative shear stress-strain curves for each region. ....	9
Figure 6 - Mesoscale tensile stress-strain curves of various gauges widths in FeCrAl C26M. ....	11
Figure 7 - (a) SEM overview of the mesoscale tensile bars cut in the C26M weld specimen. Comparison of the (b) engineering stress-strain curves, (b) tensile yield and ultimate strength, and (d) uniform elongation and tensile ductility measured in each region. ....	12
Figure 8 - Comparison of the (a) nanoindentation hardness, (b) nanoindentation yield strength, (c) micropillar yield strength, and (d) microshear yield for selected weld regions.....	13

TABLES

Table 1. Chemical composition of FeCrAl C26M alloy. .... 2

Table 2 - Summary of the micromechanical properties in each region of the weld..... 13

Table 3 - Summary of the mesotensile properties in each region of the weld. .... 14

Intentionally Blank



## 1. Introduction

Among several candidates for “accident tolerant” fuel cladding, FeCrAl alloys are among the top choices due to their superior high temperature oxidation resistance, aqueous corrosion resistance, low radiation-induced swelling, and tolerance to loss-of-coolant accident conditions [1-4]. It is important to note that despite their higher neutron absorption cross-section compared to zirconium-based alloys, their mechanical and chemical stability over a range of environment make this alloy an attractive candidate to others (i.e. SiC-based cladding). Ongoing work at Oak Ridge National Lab has focused on a composition optimized FeCrAl alloy for tube processing and deployment into light water reactors [5]. Recent testing has resulted in one alloy being down-selected for such use: C26M.

As part of a fuel assembly, FeCrAl tubes are typically welded to a threaded plug which is used to fix their position within a fuel bundle. For this particular alloy, tungsten inert gas (TIG) welding was chosen due to its extensive history of use in tube welding and simple setup needed to join the parts. To date, little mechanical evaluation has been performed on welded C26M alloys.

Evaluating performance under neutron irradiation is a time consuming process that requires years of irradiation to reach desired doses. If a variety of heats and joining processes are to be explored to reach an optimized assembly, the cost for commitment into a reactor can become significant (>10 years). Ion irradiation, often used as a surrogate to neutron irradiation, offers a solution as a screening tool that has significantly higher dpa rates and does not activate the material, resulting in significantly lower costs for material evaluation. Ion irradiation has been used to simulate a variety of radiation effects in materials, including radiation-induced hardening in FeCrAl alloys [6-11]. However, one major downside to ion irradiation is the limited irradiated volume by the ion, typically within 2  $\mu\text{m}$  of the incident surface for MeV heavy ions and <100  $\mu\text{m}$  for MeV light ions. Investigating the mechanical property changes to ion irradiated volumes generally requires microscale techniques, with a few irradiations (i.e. light ion) permitting mesoscale mechanical testing.

In this study, the primary objective is to understand and evaluate the mechanical properties of the C26M weld at both the microscale and mesoscale. Microscale techniques, such as nanoindentation, possess superior spatial resolution compared to conventional techniques enabling a more detailed study of the system. Furthermore, microscale testing is capable of isolating light and heavy ion irradiated volumes to obtain a purely irradiated material response. Mesoscale testing balances the larger testing volume with region selectivity. That is, maintaining test specimen sizes small enough to reside with regions of interest (i.e. a heat-affected zone), but straining a large enough volume to approximate bulk tests. For mesoscale testing, higher energy light ions are the only options available for irradiation of the large testing volume.

While macroscale tensile testing is the ideal test for evaluating the weld mechanical properties, the large volume required provides limited information of the local mechanical properties in each region. Instead, we employ tensile testing on the mesoscale (sub mm) as a means of extracting tensile property data from each weld region. A variety of microscale testing including Berkovich and spherical nanoindentation, micropillar compression, single and double microshear compression are used to investigate the localized property changes in the weld regions. Mesoscale tensile results are used as a baseline for comparison and evaluation of the sensitivity for microscale tests.

## 2. Materials and Methods

A FeCrAl C26M tube and plug with a composition given in Table 1 were joined together using conventional tungsten inert gas (TIG) welding. Specimens were cut into thin pieces approximately 4 mm wide and 10 mm long. All samples were ground to a thickness of ~0.25 mm using 600 grit SiC abrasive paper. For nanomechanical and microscale mechanical testing, one surface of the specimen was further polished to a final solution of 0.04  $\mu\text{m}$  silica. For mesoscale tensile testing, both surfaces were polished to a solution of 0.25  $\mu\text{m}$  diamond, with one side polished to a final solution of 0.04  $\mu\text{m}$  silica to provide visibility of grains under an optical microscope.

**Table 1. Chemical composition of FeCrAl C26M alloy.**

Alloy ID	Fe	Cr	Al	Y	Mo	Si	Nb	C	S	O	N
C26M	80.72	13.01	6.24	0.030	-	-	-	<0.01	0.001	-	-

Electron backscatter diffraction was performed on the outer surface of the joined tube and plug using a FEI Inspect operated at 20 kV equipped with an EDAX detector. A FEI Helios focused ion beam (FIB) mill operated at 30 kV was used to form the micropillars and microshear specimens. Micropillars were fabricated to have a nominal diameter of 5  $\mu\text{m}$  and a height of 12  $\mu\text{m}$ . Single microshear pillars were fabricated in a similar manner as given in [1], such that the shear region had a width of 2  $\mu\text{m}$ , thickness of 3  $\mu\text{m}$ , and height of 8  $\mu\text{m}$  and was etched at 45 degrees to the surface. Double shear specimens had a similar geometry to those in [13], with the same shear region geometry for both shear zones. Micro-compression of the micropillar and microshear specimens was performed using a Hysitron PI-85 equipped with a 20  $\mu\text{m}$  diamond flat punch. Deformation was observed *in situ* in a FEI Magellan operated at 5 kV. Both micropillar and microshear specimens were compressed at a strain rate of  $2 \times 10^{-2}$  1/s. The microcompression testing with pillars and shear specimens were all placed in grains oriented near the (111) plane. For shear specimens, this ensures that the slip plane can be aligned parallel to the shear region and result in confined shear loading. Some micropillars are fabricated in the same grains as the shear specimens, providing a more fair comparison of the results.

Nanoindentation tests were performed on a Keysight G200 Nanoindenter with a diamond Berkovich tip to a final displacement of 2,000 nm with a constant strain rate (loading rate divided by the load) of  $0.05 \text{ s}^{-1}$ . Continuous stiffness measurements (CSM) were performed at a frequency of 45 Hz and 2 nm displacement amplitude. Hardness and modulus measurements were determined using the Oliver-Pharr method [14]. The tip area function was calibrated by indenting fused silica and using tip properties with a Young's modulus and Poisson's ratio of 1130 GPa and 0.07 (diamond). Spherical nanoindentation tests were performed using a spherical tip with a radius of 100  $\mu\text{m}$  radii. Nanoindentation was performed to a depth of 500 nm using similar system parameters to the nanoindentation with a Berkovich tip. Analysis was performed using a technique outlined by Pathak and Kalidindi [15]. Due to the high throughput nature of the tests, both nanoindentation with a Berkovich and spherical tip were performed blindly. That is, arrays of indents were placed without regards to the orientation of the matrix.

Mesoscale tensile specimens were cut using a FemtoScribe laser system located at the Center for Integrated Nanotechnologies at Los Alamos National Lab. The FemtoScribe houses a Coherent Monaco laser and was operated with a pulse width of 350 fs, wavelength of 1055 nm, repetition rate of 30 kHz, and average energy of 12  $\mu\text{J}$ . Microtensile bars were cut to a gauge width of ~90  $\mu\text{m}$ , gauge thickness of ~90  $\mu\text{m}$ , and gauge length of ~400  $\mu\text{m}$ . At least one set of

four tensile bars was fabricated in each weld region, with multiple sets produced in the tube and plug base materials. Mesotensile bars were fabricated and pulled sequentially, starting in the plug base material and proceeding through all weld regions into the tube base material. Mesotensile bars were pulled at a strain rate of  $2.5 \times 10^{-2}$  1/s. Due to the small laser-induced damage region in the material, no additional processing after laser cutting was performed [16].

### 3. Results and Discussion

#### 3.1 Microstructure of the FeCrAl weld

Figure 1 shows an inverse pole figure map generated from the polished surface of the weld. The weld region spans a width of approximately 2 mm, providing ample room for a variety of micro- and mesoscale mechanical testing. From Fig. 1 there are a few notable observations to be made. First, the fusion zone (FZ) extends deeper into the tube side than the plug. This is reasonable considering the fact that the plug has a larger thermal mass than the tube and therefore cools more quickly during the welding process. Second, the plug and tube are textured, favoring the (100) and (111) orientations, respectively. The plug heat-affected zone (HAZ) and tube HAZ are approximately the same width but take on a texture similar to the base material. Third, the grain size in the plug is  $\sim 70 \mu\text{m}$ , larger than the  $\sim 50 \mu\text{m}$  grain size in the tube. It follows that the grain size in the plug HAZ ( $150 \mu\text{m}$ ) is also larger than the tube HAZ ( $\sim 100 \mu\text{m}$ ).

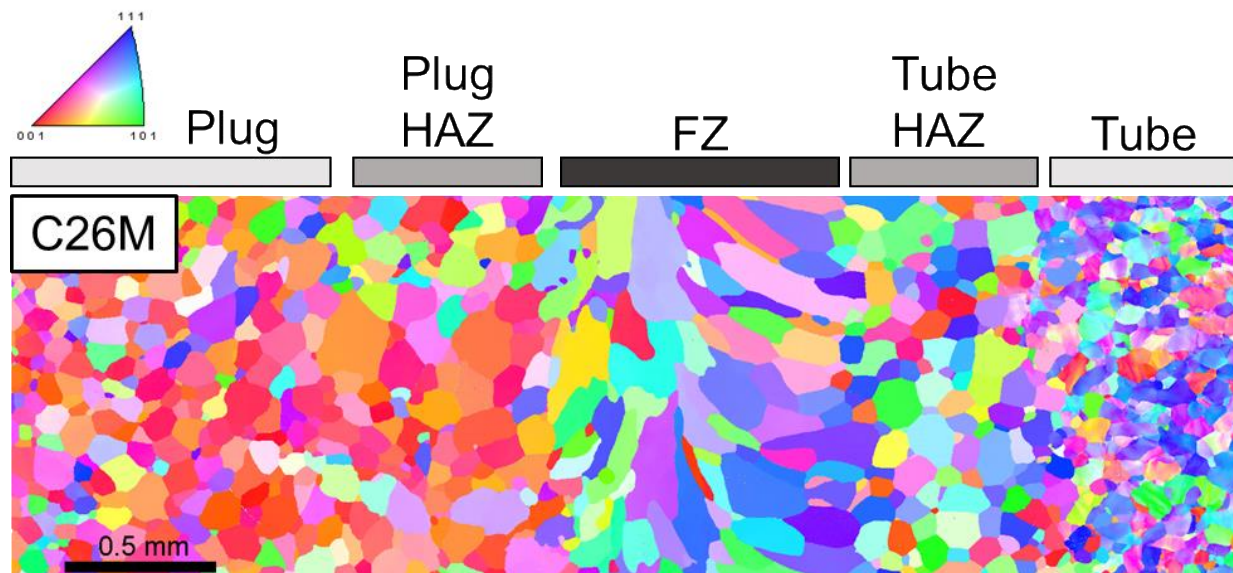


Figure 1 - EBSD pole figure map of the C26M weld

The strategy for evaluating the microscale mechanical properties of the weld specimen was to use the highest throughput techniques to determine where the more FIB-intensive mechanical tests needed to be performed:

- 1) Nanoindentation with a Berkovich tip is performed to obtain a hardness and modulus profile spanning the entire weld region and into the base materials.
- 2) Spherical indentation followed nanoindentation hardness measurements to qualitatively determine regions that contained high and low dislocation content, in addition to measuring the nanoindentation yield strength of each region.
- 3) Micropillar fabrication and compression in grains with orientations near the [111] plane normal for all weld regions. Micropillar compression is a fixed volume and more uniaxial test than the preceding nanoindentation tests and likely to be more sensitive to changes in the microstructure.

Results from nanoindentation and micropillar compression were used to isolate one side of the weld for microshear testing. Due to the significantly longer FIB time required to make one shear specimen, only the weld side that showed the largest change in mechanical properties was chosen for analysis. Both single and double shear specimens were fabricated in each region.

### 3.2 Nanoindentation hardness and modulus profiling

Nanoindentation has been widely employed to evaluate changes to welds and notably the measurement of residual stress in different regions [17-21]. The technique provides greater spatial and depth sensitivity to microstructural changes that result in variations to the hardness and modulus of the material. Many of the nanoindentation results show good agreement with conventional microhardness measurements, indicating its ability to reproduce more macroscale results.

Fig. 2 shows the nanoindentation results obtained from the FeCrAl weld. The hardness was averaged at a depth region 400-500 nm below the surface to avoid size effects from strain gradients [22-25]. The nanoindentation hardness profile in Fig. 2c suggests that the fusion zone is slightly harder than the other weld regions. Microstructural defects or residual stress (compressive) are two factors that may give rise to the increase in hardness. However, review of the load-displacement curves show differences of < 10% at 2000 nm between the base material and weld, suggesting the largest contributor to the difference are microstructural defects, such as dislocations. We acknowledge that the process of sectioning and grinding may relieve a small portion of any residual stress remaining in the material after joining, especially at the depths where nanoindentation probes. The small hardness differences highlighted in Figs. 2a and 2c, however, suggest that the residual stress in the joined material was not significant to begin with.

It is important to note that FeCrAl, a body center cubic iron alloy, is not isotropic, and will result in a variation in nanoindentation hardness and moduli based on grain orientation [26,27]. The scatter in the Figs. 2c and 2d may arise not only from differences in defect concentration (i.e. dislocation) but also from the orientations sampled. The grains in the fusion zone are significantly larger than the other weld regions and likely to result in an undersampling of grain orientations compared to the other regions. To overcome this potential issue, several nanoindentation arrays were placed randomly across each weld region (4 mm coverage) and across different samples to ensure that a sufficient number of regions were sampled. Fig. 1 shows that the plug and tube possess different textures. However, Fig. 2c suggests that this does not result in a significantly different hardness between the two base materials, highlighting the fact that microstructural defects (e.g. dislocations from cold-work) are the major contributor to the response.

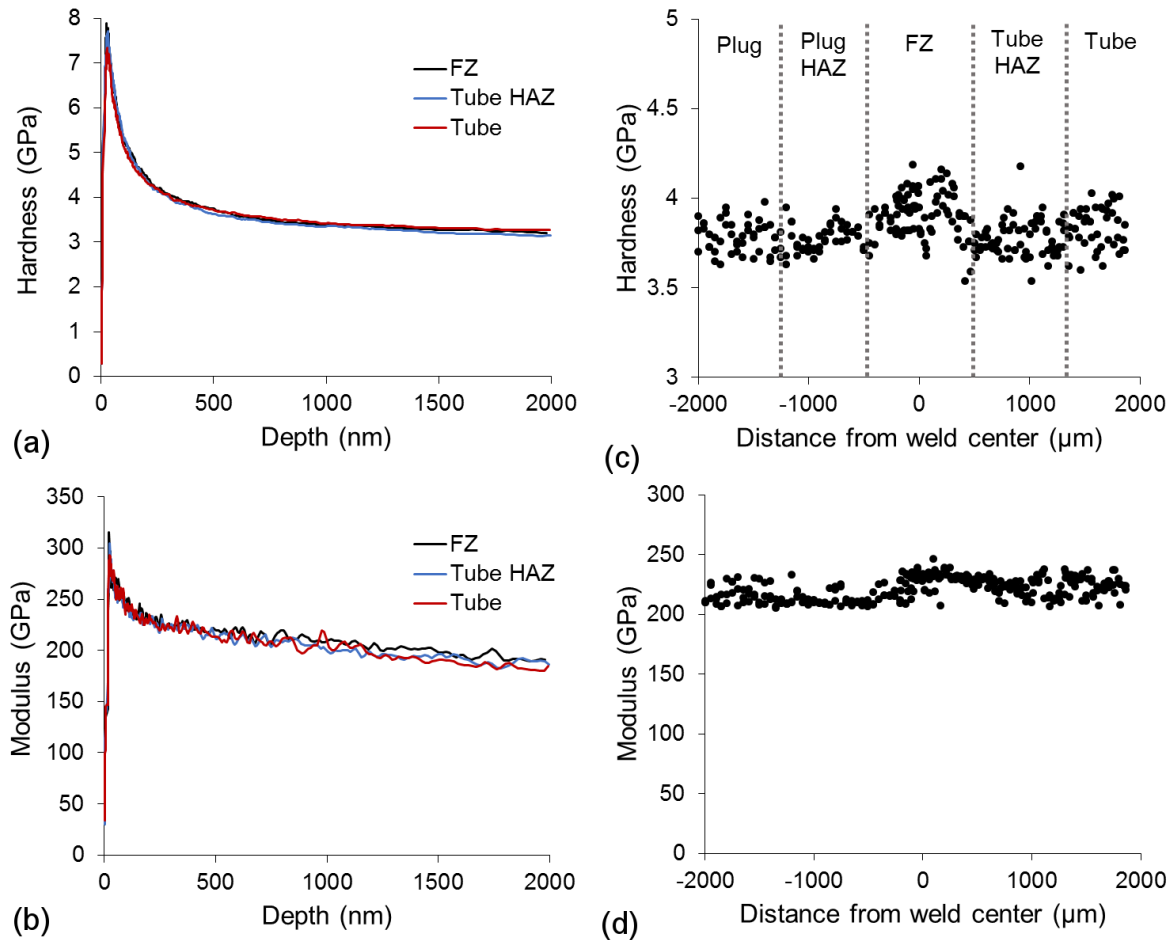


**Figure 2 - (a) Hardness and (b) Modulus depth profiles obtained from Berkovich nanoindentation in the fusion zone, tube heat-affect zone, and tube base material. (c) Hardness and (d) Modulus profiles across the C26M weld averaged between a depth of 400 nm to 500 nm.**

### 3.3 Spherical Nanoindentation

Spherical nanoindentation as a method to extract nanoindentation stress-strain curves is a relatively new technique [15]. The use of a blunt tip, such as a spherical tip, enables the recording of the elastic loading during indentation at sufficiently high strain rates to avoid instrumentation or specimen creep. Compared to sharp indenter tips, such as a Berkovich tip, the stress field generated beneath the tip is more uniform and was shown to have good agreement with uniaxial tests [28].

Fig. 3 shows representative spherical nanoindentation stress-strain curves extracted from different weld regions. Spherical nanoindentation stress-strain curves show, in some cases, a significantly higher yield strength followed by an abrupt drop in stress and increase in strain. These “pop-ins” are the result of a low dislocation source density requiring higher stresses to nucleate dislocations for plasticity [15]. These features nanoindentation stress-strain curve do not necessarily reflect the correct yield strength. One technique to reduce or eliminate pop-ins was used by Wang *et al.* [29]. Rather than using electropolishing which can create a more defect-free



surface, it was recommended to use some form of mechanical polishing with a fine particle solution as the final step to introduce defects in the near surface.

The preparation method for these specimens is similar to that outlined in [29]. Without introducing further damage to the surface, one of the only viable options for extracting yield strengths is to use a linear regression technique proposed in [30]. Here, a straight line is fit to the data after the pop-in and the intersection point on the elastic portion of the curve is taken as the yield strength. In principal, the technique has provided good agreement with specimens that do not exhibit pop-ins. We combine these techniques to extract the nanoindentation yield strengths.

Our results show considerable variation, beyond what is expected from orientations changes or from the nanoindentation hardness data [30]. As will be shown later in Fig. 8, differences between each region are inconclusive. We attribute this to the following. The method for calculating nanoindentation stress-strain curves generated several good fits to the data. Although one could subjectively pick a single curve, our method involves averaging all those curves which are above a certain fit quality threshold (e.g. R-squared). If the error associated with the linear regression is combined with the error from fitting, the result is a large range of measured yield strengths. The data, however, provides a valuable estimate to the uniaxial yield strength and is between 300 – 400 MPa.

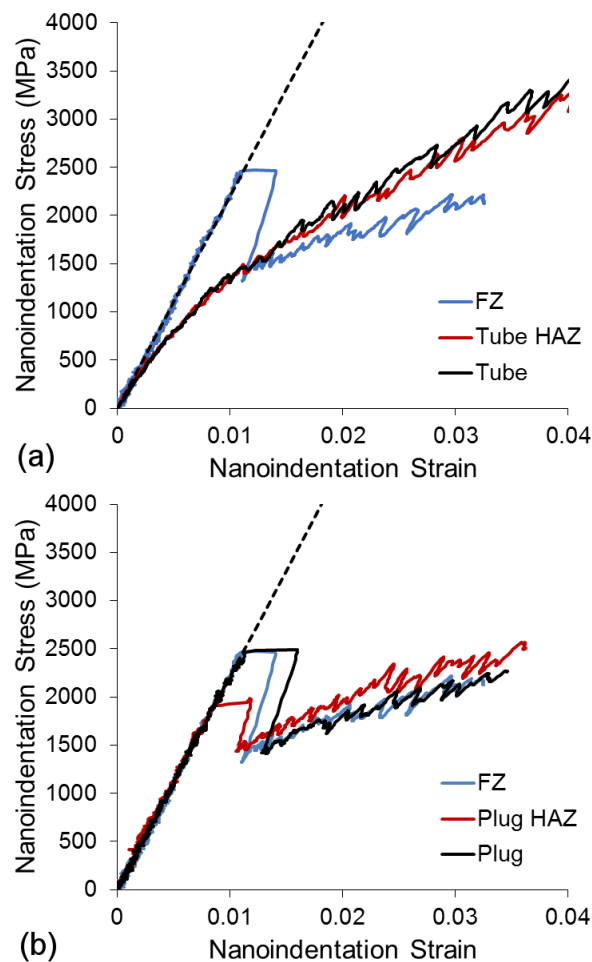


**Figure 3 - Spherical Nanoindentation stress-strain curves for the (a) tube and (b) plug side of the weld.**

### 3.4 Micropillar Compression

The nanoindentation results did not show a significant difference between the weld regions and the bulk materials that would allow one region to be down selected for a more detailed study. Therefore, micropillars were fabricated in all weld specimen regions in grains oriented near the (111) plane. In an effort to maximize both the pillar volume (to avoid size effects) and number of pillars in each grain, a nominal pillar width of 5  $\mu\text{m}$  was chosen. Even at this size, the pillar is still subject to size effects from dislocation source starvation that results in an elevated yield strength [31-36]. Nonetheless, our goal is not to obtain macroscale mechanical properties with microscale testing, but to evaluate sensitivity to differences in the weld regions.

Fig. 4 shows the results of micropillar compression in the different weld regions. Micropillars were compressed to large strain values and an illustrative before and after compression micrograph of a pillar in the fusion zone is given in Figs 4a and 4b. Figs. 4c and 4d show representative stress-strain curves obtained from micropillar compression in each region. To avoid undersampling the response, micropillars were fabricated in different grains. For the case of the fusion zone, the grain selected spanned a large area (0.3 mm) and micropillars were fabricated at different locations in the grain.

The differences between each region are clear, especially at low strain values. The plug and plug HAZ appear to have the lowest yield strength ( $\sim 600$  MPa) and followed closely by the tube. The tube HAZ and FZ both possess higher yield strengths than the other regions. On the other hand, the plug, plug HAZ, and tube show the greatest amount of work hardening compared to the tube HAZ and FZ. Compared to nanoindentation, micropillar compression is not sensitive to residual stress. This is due to the fact that the process of etching the island via FIB removes any residual stress present in the region [37]. Thus, the variations in the micropillar response are due entirely to the differences in microstructure.

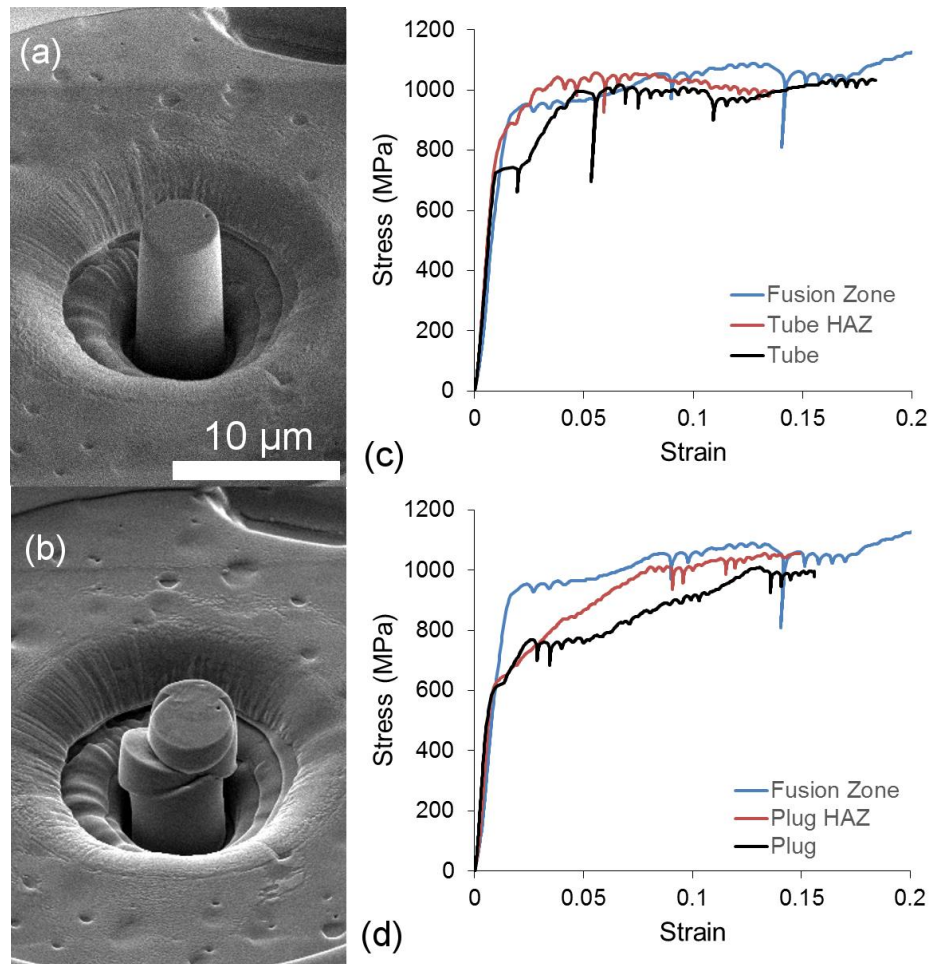


**Figure 4 - Micropillar in the fusion zone (a) before and (b) after compression. Micropillar stress-strain curves for the (a) tube and (b) plug side.**

### 3.5 Microshear Compression

Microshear compression testing utilized in this study builds upon earlier studies that employed single and double shear specimens to investigate a variety of mechanical properties [13,38]. From the microshear compression results, the plug side clearly shows the greatest change in yield strength across the weld region and therefore the focus for microshear testing is on the plug side of the weld. Single shear and double shear specimens were fabricated with principally three objectives. First, single shear specimens, similar to micropillars, are insensitive to residual stress and their response is due purely to the microstructure. Double shear pillars, on the other hand, are sensitive to residual stress, as they are not fully isolated from the stressed surface, and will have a response that is a combination of both residual stress and microstructural effects.

Second, shear in this orientation permits direct loading of the slip planes in bcc FeCrAl (i.e. Schmid factor of  $\sim 1$ ). This configuration has a more localized stress field. This translates into a system that is not influenced strongly by boundary effects of the structure (i.e. dislocation pile-up at supports). The result is a system that is capable of achieving high shear strain values



compared to other orientations. Third, if any embrittlement or loss of ductility results from the welding process, compression to high shear strains will result in the eventual failure of and significant differences in fracture shear strain between the shear specimens in different regions.

Fig. 5 provides a comparison of the single and double shear response in the plug side regions of the weld. Figs. 5e and 5f show that the double shear yield strengths are larger in comparison to single shear specimens. Furthermore, nearly all double shear specimens show larger strain hardening compared to the single shear specimens. These differences might suggest that there is some amount of residual stress influencing the double shear responses. However, such an interpretation requires careful consideration of other factors influencing the response.

The double shear specimen response includes two shear regions separated by  $20\text{ }\mu\text{m}$ . In a number of the grains examined, the double shear specimen length spanned nearly two thirds of the grain diameter. This translates to a strong possibility that each shear region contained a different defect density, and is supported by the asymmetric response of compressed double shear specimens in Fig. 5d. This response, in turn, would result in more strain hardening by one shear region blocking low stress specimen deformation while the necessary stress was being reached in that shear region to induce plastic flow. Furthermore, at high strain values  $>1.5$ , compression of double shear specimens led to eventual failure in the plug base material. No other shear specimens in any other shear region showed this result.

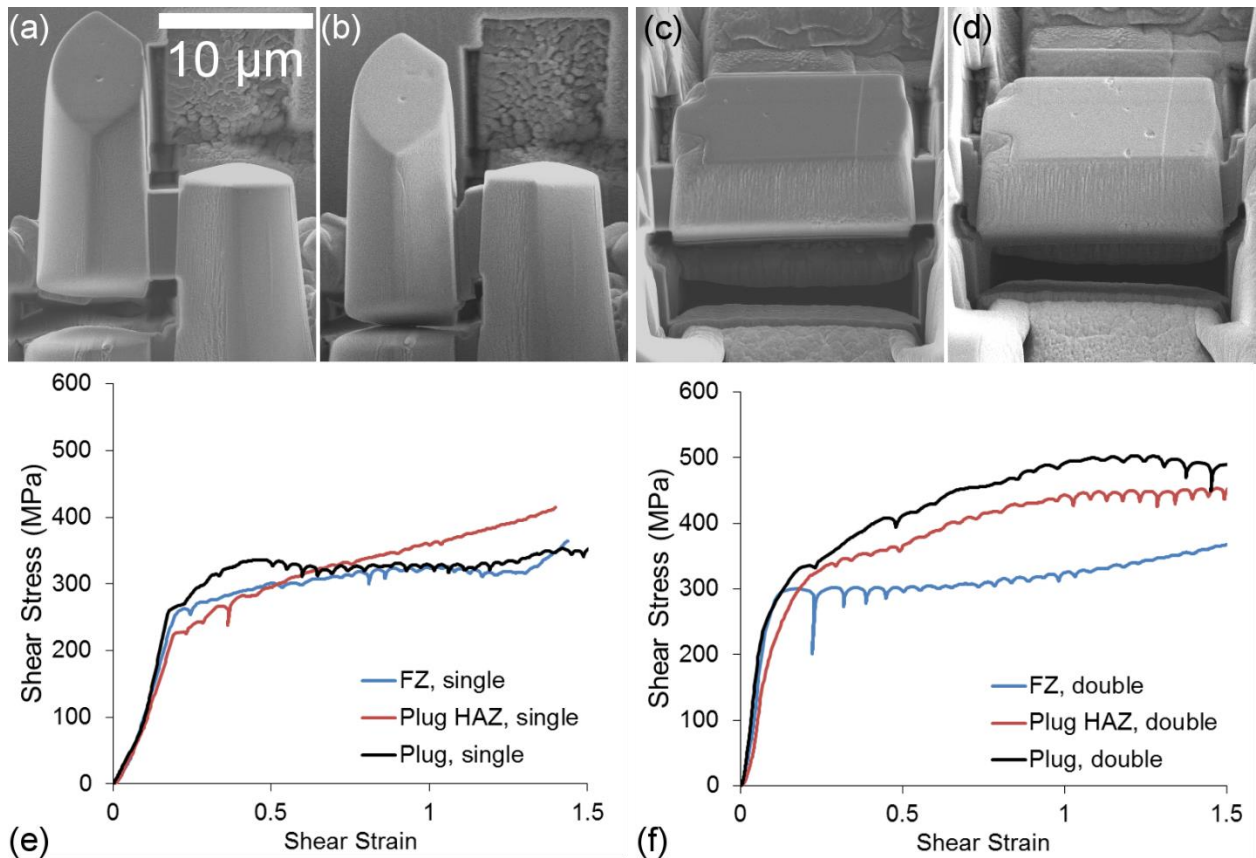


**Figure 5 - Single shear (a) before and (b) after compression, and (c) representative shear stress-strain curves for each region. Double shear (d) before and (e) after compression, and (f) representative shear stress-strain curves for each region.**

### 3.6 Microshear Compression

Mesoscale mechanical testing is a comparatively under-utilized technique due principally to the difficulty of fabricating specimens on this scale. Machining specimens is only viable through a handful of techniques: plasma FIB, micro-wire electrodischarge machining, laser machining [39-43]. Plasma FIB systems utilize a specialized ion source to deliver high ion currents to the target material. These machines typically require an expensive, complementary electron microscopy system to be used effectively and have limited ability to remove material to depths exceeding 50  $\mu\text{m}$  in a few hours. Micro-wire EDM has a significantly higher throughput but is accompanied by several major disadvantages: the specimen must be sufficiently conductive, feature sizes smaller than the wire diameter are generally not machinable, and the resulting large heat-affected region must be removed.

Femtosecond laser machining utilizes ultrafast pulses of light to remove material with minimal damage. Since the interaction time with the material is much faster than the thermalization time of highly conductive metals, minimal amounts of heat are deposited into the material while machining. For a range of materials, this heat-affected zone is on the order of 100 nm to 5  $\mu\text{m}$  [16,43]. Small structures require post-processing to remove this region. However, the tensile bars in this study are sufficiently large such that the  $\sim 1$   $\mu\text{m}$  damage region induced by laser machining will have a negligible effect on the mechanical properties.

Before a mesotensile geometry is chosen for the weld analysis, a short investigation into the influence of a variation in the gauge area on the tensile properties was performed on a separate tube heat of FeCrAl. Here, all gauge thicknesses and lengths were fixed to 80  $\mu\text{m}$  and 400  $\mu\text{m}$ , respectively. Fig. 6 shows a comparison of the tensile properties with variations to the gauge width. While there are variations to the tensile yield and ultimate strengths, these are attributable to the fact that smaller tensile bars contain, at most, a few grain boundaries and subject more strongly to variations in the microstructure (i.e. variations in dislocation content between grains). All specimens are within reasonable agreement with bulk tensile data reported in a prior study [44], with the exception to the yield strength. This is due to the fact that tensile bars contain only a few grain boundaries and may, for smaller widths, exhibit single crystal response. Based on Fig. 6, our selection of a gauge width of 90  $\mu\text{m}$  and a thickness of 90  $\mu\text{m}$  is a reasonable choice.

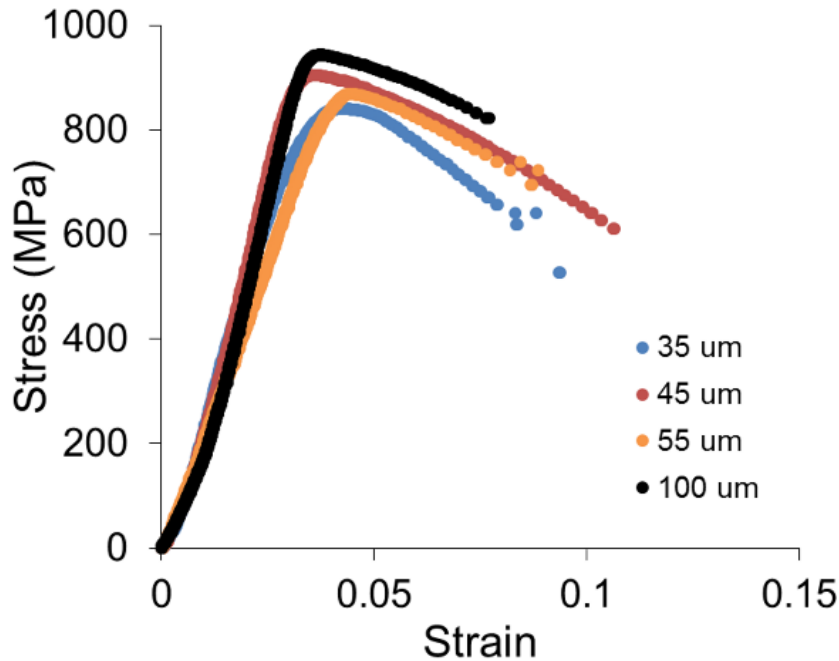


**Figure 6 - Mesoscale tensile stress-strain curves of various gauge widths in FeCrAl C26M.**

Fig. 7 shows the results of mesoscale tensile testing in the different weld regions. The results show that the tube base material has an exceptionally high tensile yield and ultimate strength compared to the other regions. We attribute this observation to the cold-work present in the tube region that is visible as in grain misorientation in Fig. 1. However, the most striking result from the testing is that the FZ possesses the largest uniform elongation (10%) and tensile ductility (20%) while the plug HAZ has the lowest of such properties. The majority of specimens have yield strengths on the order of 300 MPa and ultimate tensile strengths between 350-400 MPa. Uniform elongations vary from 6% (plug HAZ) to 10% (FZ), with ductility varying from 12% to 20%. Fig. 7c and 7d combined together paint a very clear picture of the expected macroscale response: failure will occur in the plug HAZ as it is both the weakest and least ductile of all the regions.

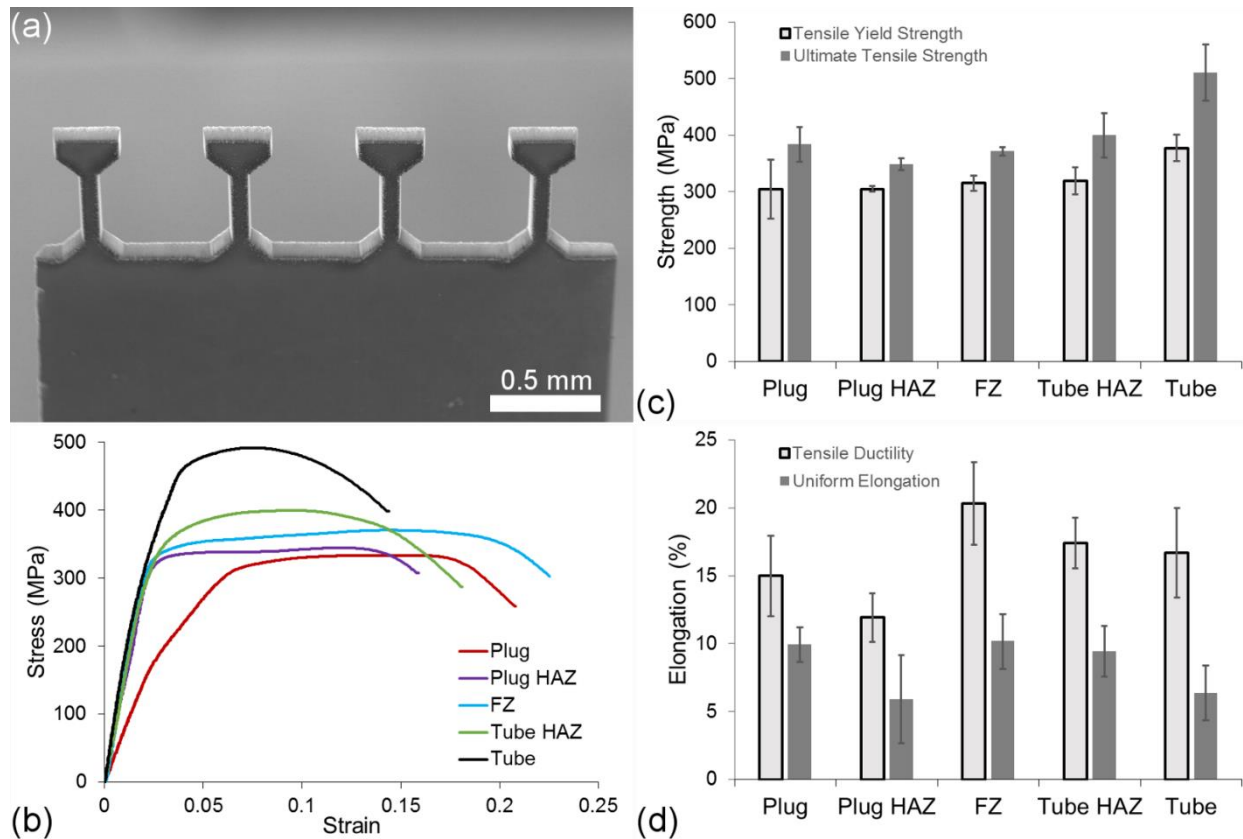


**Figure 7 - (a) SEM overview of the mesoscale tensile bars cut in the C26M weld specimen. Comparison of the (b) engineering stress-strain curves, (b) tensile yield and ultimate strength, and (d) uniform elongation and tensile ductility measured in each region.**

### 3.7 Microshear Compression

Fig. 8 provides a comparison of the hardness and yield strengths measured using each of the microscale tests performed. Tables 2 and 3 contain a summary of all of the mechanical properties measured from the various tests in this study. Compared to the microcompression tests, nanoindentation (Fig. 8a and 8b) both show low sensitivity to microstructural differences in the different weld regions. If one indentation test were to be chosen, strictly due to low cost associated with the tests, nanoindentation with a Berkovich tip to extract hardness would be the top choice due to both the ease of analysis and repeatability of results.

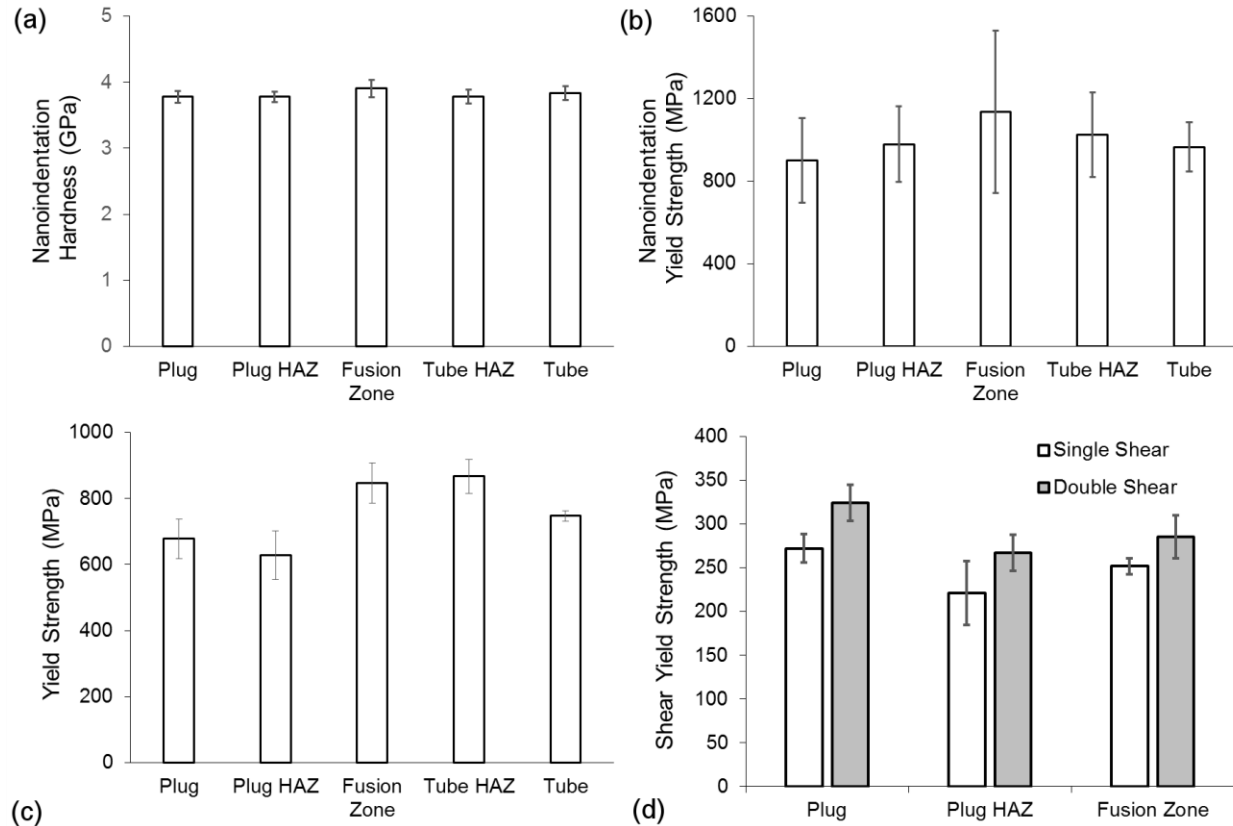


**Figure 8 - Comparison of the (a) nanoindentation hardness, (b) nanoindentation yield strength, (c) micropillar yield strength, and (d) microshear yield for selected weld regions.**

**Table 2 - Summary of the micromechanical properties in each region of the weld.**

Region	Modulus (GPa)	Hardness (GPa)	Nanoindentation Yield Strength (GPa)	Compression Yield Strength (GPa)	Single Shear Yield Strength (GPa)	Double Shear Yield Strength (GPa)
<b>Tube</b>	$225 \pm 7.6$	$3.83 \pm 0.11$	$0.97 \pm 0.12$	$0.75 \pm 0.02$	-	-
<b>Tube HAZ</b>	$221 \pm 7.6$	$3.78 \pm 0.10$	$1.02 \pm 0.20$	$0.87 \pm 0.05$	-	-
<b>Fusion Zone</b>	$227 \pm 8.0$	$3.90 \pm 0.13$	$1.14 \pm 0.39$	$0.85 \pm 0.06$	$0.25 \pm 0.01$	$0.29 \pm 0.02$
<b>Plug HAZ</b>	$213 \pm 5.6$	$3.78 \pm 0.08$	$0.98 \pm 0.18$	$0.63 \pm 0.07$	$0.22 \pm 0.04$	$0.27 \pm 0.02$
<b>Plug</b>	$215 \pm 7.6$	$3.78 \pm 0.09$	$0.90 \pm 0.20$	$0.68 \pm 0.06$	$0.27 \pm 0.02$	$0.32 \pm 0.02$

**Table 3 - Summary of the mesotensile properties in each region of the weld.**

<b>Region</b>	<b>Tensile Yield Strength (GPa)</b>	<b>Ultimate Tensile Strength (GPa)</b>	<b>Uniform Elongation (%)</b>	<b>Tensile Ductility (%)</b>
<b>Tube</b>	$0.38 \pm 0.02$	$0.51 \pm 0.05$	$6.35 \pm 2.02$	$16.7 \pm 3.30$
<b>Tube HAZ</b>	$0.32 \pm 0.02$	$0.40 \pm 0.04$	$9.43 \pm 1.88$	$17.4 \pm 1.87$
<b>Fusion Zone</b>	$0.32 \pm 0.01$	$0.37 \pm 0.08$	$10.2 \pm 2.02$	$20.3 \pm 3.06$
<b>Plug HAZ</b>	$0.31 \pm 0.01$	$0.35 \pm 0.01$	$5.90 \pm 3.24$	$11.9 \pm 1.79$
<b>Plug</b>	$0.31 \pm 0.05$	$0.38 \pm 0.03$	$9.94 \pm 1.28$	$15.0 \pm 2.95$

The micropillar and microshear compression testing both show similarities in the trends observed in mesoscale tensile testing. Despite the elevated yield strengths measured due to size effects, both tests communicate the same message: the plug HAZ has the lowest yield strength. However, the micropillar yield strengths best match the tensile yield and ultimate strength obtained from mesotensile tests (Fig. 8c). Although likely coincidental, the trends also match the elongation trends in Fig. 8d.

The conclusion from the microscale tests and comparison against mesotensile results would suggest that micropillar compression is the tool best suited for evaluating the mechanical properties of this particular C26M weld on the microscale. Compared to the sensitivity of the shear specimens and the amount of time needed to fabricate such specimens, micropillars would appear to be a natural choice. This, however, is based on the evaluation of a weld with little residual stress present.

One important aspect of mesotensile tensile testing is that the sequential sectioning of tensile bars into different weld regions has the potential to relieve residual stress present in the various regions. While these tensile bars are attached to the specimen at one end, it is likely that after etching a new set, some or all of the residual stress present in the neighboring region may be relieved. It is also worth noting that the thicknesses routinely tested ( $90\ \mu\text{m}$ ) are much thinner than the starting joined material. Sectioning and polishing the specimen may also alleviate residual stress through the bending of the thin polished specimen. No such behavior was observed in the specimens prepared, further indicating a minimal residual stress present in the joined materials.

The recommendation from the following tests can be summarized as follows:

- Nanoindentation with a Berkovich tip should be performed first to quickly evaluate differences in the weld regions. Residual stress can also be identified and calculated here according to [19].
- If residual stresses are present, a combined single shear and double shear specimen would enable evaluation of the mechanical properties with and without residual stress influencing the result.
- If little or no residual stresses are present, micropillar compression is best suited for probing weld mechanical properties.

- Mesotensile testing should be performed when possible to extract significantly more information on weld properties, including ductility information not easily derived from the microscale tests.

#### **4. Conclusions and Future Work**

In this study, the mechanical properties of a FeCrAl C26M weld were evaluated using a variety of microscale and mesoscale techniques. Nanoindentation did not prove to be very sensitivity to microstructural differences in each weld region. Nanoindentation hardness measurements obtained using a Berkovich tip are recommended due the lower variability in hardness values and potential sensitivity to residual stress.

Among the targeted microscale mechanical tests, micropillar compression was observed to be the most sensitive to change in the microstructure. Differences between single and double microshear compression likely arose from the asymmetric deformation of the two shear regions in the double shear specimen.

Mesoscale tensile testing was performed in each weld region. Comparison of the elongation and strengths of the regions show clearly that during loading of the weld material, the plug heat-affected zone is the weakest and will determine failure of the material. Using the mesotensile results as a baseline for comparison, micropillar compression was found to match the mesotensile trends the best for the C26M weld investigated in this study. However, single and double shear testing should not be discounted, especially if residual stresses are present.



## 5. References

1. R.B. Rebak, K.A. Terrani, W.P. Gassmann, J.B. Williams, K.L. Ledford. Improving Nuclear Power Plant Safety with FeCrAl Alloy Fuel Cladding, *MRS Advances* (2017) 1-8.
2. Y. Yamamoto, B.A. Pint, K.A. Terrani, K.G. Field, Y. Yang, L.L. Snead. Development and property evaluation of nuclear grade wrought FeCrAl fuel cladding for light water reactors, *J Nucl Mater* 467, Part 2 (2015) 703-716.
3. K.G. Field, M.N. Gussev, Y. Yamamoto, L.L. Snead. Deformation behavior of laser welds in high temperature oxidation resistant Fe–Cr–Al alloys for fuel cladding applications, *J Nucl Mater* 454 (2014) 352-358.
4. S.J. Zinkle, K.A. Terrani, L.L. Snead. Motivation for utilizing new high-performance advanced materials in nuclear energy systems, *Current Opinion in Solid State and Materials Science* 20 (2016) 401-410.
5. Y. Yamamoto, Z. Sun, B.A. Pint, K.A. Terrani. Optimized Gen-II FeCrAl cladding production in large quantity for campaign testing. Oak Ridge: Oak Ridge National Laboratory, 2016.
6. E. Aydogan, J.S. Weaver, S.A. Maloy, O. El-Atwani, Y.Q. Wang, N.A. Mara, *Journal of Nuclear Materials*, 503 (2018) 250-262.
7. T. Chen, J. G. Gigax, L. Price, D. Chen, S. Ukai, E. Aydogan, S. A. Maloy, F. A. Garner, L. Shao, Temperature dependent dispersoid stability in ion-irradiated ferritic-martensitic dual-phase oxide-dispersion-strengthened alloy: Coherent interfaces vs. incoherent interfaces, *Acta Mater.* 116 (2016) 29-42.
8. J. G. Gigax, H. Kim, T. Chen, F. A. Garner, L. Shao, Radiation instability of equal channel angular extruded T91 at ultra-high damage levels, *Acta Mater.* 132 (2017) 10-19.
9. E. Aydogan, S. A. Maloy, O. Anderoglu, C. Sun, J. G. Gigax, L. Shao, F. A. Garner, I. E. Anderson, J. J. Lewandowski, Effect of tube processing methods on microstructure, mechanical properties and irradiation response of 14YWT nanostructured ferritic alloys, *Acta Mater.* 134 (2017) 116-127.
10. H. Kim, J. G. Gigax, T. Chen, S. Ukai, F. A. Garner, L. Shao, Dispersoid stability in ion irradiated oxide-dispersion-strengthened alloy, *J. Nucl. Mater.* 509 (2018) 504-512.
11. J. S. Weaver, S. Pathak, A. Reichardt, H. T. Vo, S. A. Maloy, P. Hosemann, N. A. Mara, Spherical nanoindentation of proton irradiated 304 stainless steel: A comparison of small scale mechanical test techniques for measuring irradiation hardening, *J. Nucl. Mater.* 493 (2017) 368-379.
12. J. G. Gigax, J. K. Baldwin, C. J. Sheehan, S. A. Maloy, N. Li, Microscale shear specimens for evaluating the shear deformation in single-crystal and nanocrystalline Cu and at Cu-Si interfaces, *J. Mater. Res* 34 (2019) 1574-1583.
13. J. K. Heyer, S. Brinckmann, J. Pfitzing-Micklich, and G. Eggeler, Microshear deformation of gold single crystals. *Acta Mater.* 62 (2014) 225-238.
14. W.C. Oliver, G.M. Pharr. Measurement of hardness and elastic modulus by instrumented indentation: Advances in understanding and refinements to methodology, *J Mater Res* 19 (2004) 3-20.
15. S. Pathak, S. R. Kalidindi. Spherical nanoindentation stress-strain curves. *Mater. Sci. Eng. R* 91 (2015) 1-36.



16. J. G. Gigax, H. Vo, Q. McCulloch, M. Chancey, Y. Wang, S. A. Maloy, N. Li, P. Hosemann, Micropillar compression response of femtosecond laser-cut single crystal Cu and proton irradiated Cu, *Scripta Mater.* 170 (2019) 145-149.
17. P. Maier, A. Richter, R. G. Faulkner, R. Ries, Application of nanoindentation technique for structural characterisation of weld materials, *Mater. Char.* 48 (2002) 329-339.
18. V. H. Baltazar Hernandez, S. K. Panda, M. L. Kuntz, Y. Zhou, Nanoindentation and microstructure analysis of resistance spot welded dual phase steel, *Mater. Lett.* 65 (2010) 207-210.
19. C. A. Charitidis, D. A. Dragatogiannis, E. P. Koumoulos, I. A. Kartsonakis, Residual stress and deformation mechanism of friction stir welded aluminum alloys by nanoindentation, *Mater. Sci. Eng. A* 540 (2012) 226-234.
20. F. Legendre, S. Poissonnet, P. Bonnaillie, L. Boulanger, L. Forest, Some microstructural characterisations in a friction stir welded oxide dispersion strengthened ferritic steel alloy, *J. Nucl. Mater.* 386-388 (2009) 537-539.
21. M. Cabibbo, A. Forcellese, M. El Mehtedi, M. Simoncini, Double side friction stir welding of AA6082 sheets: Microstructure and nanoindentation characterization, *Mater. Sci. Eng. A* 590 (2014) 209-217.
22. W.D. Nix and H. Gao, Indentation size effects in crystalline materials: a law for strain gradient plasticity, *J. Mech. Phys. Solids* 46 (1998) 411-425
23. H. Gao, Y. Huang, W.D. Nix, J.W. Hutchinson, Mechanism-based strain gradient plasticity – I. Theory, *J. Mech. Phys. Solids* 47 (1999) 1239-1263.
24. Y. Huang, Z. Xue, H. Gao, W. D. Nix, Z.C. Xia, A study of microindentation hardness tests by mechanism-based strain gradient plasticity, *J. Mater. Res.* 15 (2000) 1786-1796.
25. K. Durst, B. Backes, O. Franke, M. Goken, Indentation size effect in metallic materials: Modelling strength from pop-in to macroscopic hardness using geometrically necessary dislocations, *Acta Mater.* 54 (2006) 2547-2555.
26. N. A. Stelmashenko, M. G. Walls, L. M. Brown, YU. V. Milman, Microindentations on W and Mo Oriented Single Crystals: An STM Study, *Acta Metall. Mater.* 41 (1993) 2855-2865.
27. Y. Liu, S. Varghese, J. Ma, M. Yoshino, H. Lu, R. Komanduri, Orientation effects in nanoindentation of single crystal copper, *Int. J. Plast.* 24 (2008) 1990-2015.
28. D.K. Patel, S.R. Kalidindi. Correlation of spherical nanoindentation stress-strain curves to simple compression stress-strain curves for elastic-plastic isotropic materials using finite element models. *Acta Mater.* 112 (2016) 295-302.
29. Z. Wang, H. Bei, E. P. George, G. M. Pharr. Influences of surface preparation on nanoindentation pop-in in single-crystal Mo. *Scripta Mater.* 65 (2011) 469-472.
30. J. S. Weaver, M. W. Priddy, D. L. McDowell, S. R. Kalidindi, On capturing the grain-scale elastic and plastic anisotropy of alpha-Ti with spherical nanoindentation and electron back-scattered diffraction, *Acta Mat.* 117 (2016) 23-34.
31. D. Kiener, C. Motz, G. Dehm, Micro-compression testing: A critical discussion of experimental constraints, *Mater. Sci. Eng. A* 505 (2009) 79-87.
32. J.Y. Kim and J. Greer, Size-dependent mechanical properties of molybdenum nanopillars, *Appl. Phys. Lett.* 93 (2008) 101916.
33. C. P. Frick, B.G. Clark, S. Orso, A.S. Schneider, E. Arzt, Size effect on strength and strain hardening, A.S. Budiman, S.M. Han, J. R. Greer, N. Tamura, J. R. Patel, and W.D. Nix, A

- search for evidence of strain gradient hardening in Au submicron pillars under uniaxial compression using synchrotron X-ray microdiffraction, *Acta Mater.* 56 (2008) 602-608.
34. J.Y. Kim, D. Jang, J. R. Greer, Tensile and compressive behavior of tungsten, molybdenum, tantalum and niobium at the nanoscale, *Acta Mater.* 58 (2010) 2355-2363.
35. M.D. Uchic, D. M. Dimiduk, J. N. Florando, W.D. Nix, Sample dimensions influence strength and crystal plasticity, *Science* 305 (2004) 986-989.
36. J. R. Greer, W. C. Oliver, W. D. Nix, Size dependence of mechanical properties of gold at the micron scale in the absence of strain gradients, *Acta Mater.* 53 (2005) 1821-1830.
37. A. M. Korunsky, M. Sebastini, E. Bemporad, Focused ion beam ring drilling for residual stress evaluation, *Mater. Lett.* 63 (2009) 1961-1963.
38. N. Wierczorek, G. Laplanche, J.-K. Heyer, A. B. Parsa, J. Pfetting-Micklich, and G. Eggeler, Assessment of strain hardening in copper single crystals using in situ SEM microshear experiments. *Acta Mater.* **113**, 320-334 (2016).
39. N.S. Smith, W.P. Skoczylas, S.M. Kellogg, D.E. Kinion, P.P. Tesch, O. Sutherland, A. Aanesland, R.W. Boswell, *J. Vac. Sci. Technol. B* 24 (2006) 2902–2906.
40. M.D. Uchic, D.M. Dimiduk, *Mater. Sci. Eng. A* 400-401 (2005) 268–278.
41. T. Kawakami, M. Kunieda, *CIRP Ann. Manuf. Technol.* 54 (1) (2005) 167–170.
42. M.J. Pfeifenberger, M. Mangang, S. Wurster, J. Reiser, A. Hohenwarter, W. Pfleging, D. Kiener, R. Pippan, *Mater. and Design* 121 (2017) 109-118.
43. M.P. Echlin, M.S. Titus, M. Straw, P. Gumbsch, T.M. Pollock, *Acta Mater.* 124 (2017) 37-46.
44. B. Eftink, C. Cady, T. Saleh, Tensile Testing of Generation II FeCrAl Tubing, Los Alamos: Los Alamos National Lab, 2018.